INTERNATIONAL JOURNAL FOR NUMERICAL METHODS IN FLUIDS
Int. J. Numer. Meth. Fluids **28**: 47–72 (1998)

LARGE EDDY SIMULATION OF TEMPORALLY DEVELOPING JUNCTURE FLOWS

MADHU SREEDHAR[1] AND FRED STERN*

Iowa Institute of Hydraulic Research, University of Iowa, Iowa City, IA 52242-1585, USA

SUMMARY

Large eddy simulation (LES) results are reported for temporally developing solid–solid and solid–rigid-lid juncture flows. A MacCormack-type scheme that is second-order in time, and fourth-order in space for the convective terms and second-order in space for the viscous terms, is used. The simulations are obtained for a low subsonic Mach number. The subgrid-scale stresses (SGS) are modeled using the dynamic modeling procedure. The turbulent flow field generated on a flat-plate boundary layer is used to initialize the juncture flow simulations. The results of the flat-plate boundary layer simulations are validated with experimental and direct numerical simulations (DNS) data. In juncture flow simulations, the presence of an adjacent solid-wall/rigid-lid boundary altered the mean and the turbulent field, setting up gradients in the anisotropy of normal Reynolds stresses resulting in the formation of turbulence-induced secondary vortices. The relative size of these secondary vortices and the distribution of mean and turbulent quantities are in qualitative agreement with the experimental observations for the solid–solid juncture. The overall distribution of the mean and turbulence quantities showed close resemblance between the solid–solid and the solid–rigid-lid junctures; except for the absence of a second vortical region near the rigid-lid boundary. In agreement with the experimental observations, it was found that the normalized anisotropy term exhibited similarity when plotted against the distance from the boundary, regardless of the type of boundary, i.e. solid-wall or rigid-lid. The turbulent kinetic energy increased near the rigid-lid boundary. While the surface normal velocity fluctuations decreased to zero at the rigid-lid boundary, the other two velocity components showed an increase in their energy, which is also consistent with the experimental observations. © 1998 John Wiley & Sons, Ltd.

KEY WORDS: large eddy simulation; juncture flows

1. INTRODUCTION

The flow field in a juncture generated by two interacting boundary layers are common in many engineering applications, e.g. ducts and wing-body-type configurations. A similar scenario occurs at the intersection of a solid-wall and a free-surface; where the boundary layer on the solid-wall interacts with the free-surface boundary layer. Examples include open channel flows and ship boundary layers. An important feature of turbulent juncture flows is the generation of Reynolds stress-induced secondary flows of Prandtl's second kind. Most of the investigations to date on this subject have been on channel flows, especially closed channel flows, where the outer flow is fully developed. Relatively very little is known regarding flows where the

---

* Correspondence to: Iowa Institute of Hydraulic Research, University of Iowa, Iowa City, IA 52242-1585, USA. Tel.: + 1 319 3355215; e-mail: frederick-stern@uiowa.edu

[1] E-mail: madhu@iihr.uiowa.edu

CCC 0271–2091/98/110047–26$17.50

Received 27 December 1996
Revised 21 August 1997

boundary layers are still developing in the region of interest. It appears that the present effort is the first numerical investigation where different types of developing juncture flows are studied. Turbulent flow was simulated in junctures formed either by two solid-walls or a solid-wall and a rigid-lid boundary; the rigid lid being an approximation for the free-surface.

The objectives of this study are: (1) to investigate the influence of solid and rigid-lid boundaries on developing turbulent boundary layers, (2) to identify the large scale secondary motions, (3) to evaluate the role of anisotropy of normal Reynolds stresses on the generation of these secondary flows and (4) to bring out the similarities and differences between the solid–solid and the solid–rigid-lid junctures. Considering the complexity and magnitude of the problem, this study is not intended to provide a final set of answers, but rather a first step in achieving the final goal of understanding the physics aiding the development of prediction tools for such flows.

For direct numerical simulations (DNS) and large eddy simulations (LES), the prescription of suitable inflow conditions has always been a challenge. In the present investigation, temporal simulations are considered where streamwise periodicity is assumed. The initial conditions for the juncture flow simulations are obtained from a turbulent flat-plate boundary layer simulation. For the subgrid-scale stresses (SGS), the dynamic modeling procedure of Germano *et al.* [1] is used.

The numerical scheme used in this study is a second-order predictor–corrector MacCormack-type compressible scheme that is fourth-order in space for convective terms and second-order for viscous terms. The simulations are obtained for a low subsonic Mach number (0.4) so that the compressiblity effects are minimal [2] and the flow is very close to the incompressible limit.

The rigid-lid boundary condition is often used and reported in the literature as a representation of a free-surface boundary with negligible waves for incompressible flows. The results indicate that this is a satisfactory approximation for compressible flows for the levels of Mach numbers considered in this study.

In view of the assumptions and approximations made, it is important that the results are validated. The boundary layer results are presented and validated for a range of grids using experimental [3] and DNS [4] data. For developing juncture flows, very little data is available and the comparisons are more qualitative in nature. The data of Kornilov and Kharitnov [5] appears to be the only available data in the literature for the developing solid–solid juncture. For developing solid–free-surface junctures, the data of Longo *et al.* [3] represent the most complete in terms of mean flow and Reynolds stress data.

The juncture flow simulations are obtained using the fully turbulent boundary layer as an initial condition. Spatial and ensemble averaging are performed to obtain the mean quantities. The results are analyzed to study the influence of the solid and rigid-lid boundaries on the turbulent boundary layer. The formation of secondary vortices and the role of Reynolds stress anisotropy are then discussed with the aid of experimental data. The presence of a scaling law for the anisotropy of the normal Reynolds stresses introduced by Longo *et al.* is confirmed. The influence of solid and rigid-lid boundaries on the turbulent kinetic energy is discussed followed by a discussion on the performance and limitations of the present implementation of the dynamic subgrid-scale model. Finally, concluding remarks are made.

2. BACKGROUND

The current status of turbulent juncture flow investigations that are relevant to the present study are reviewed. Since the initial conditions for the juncture flow simulations are obtained from a flat-plate simulation, a brief review of transitional-turbulent flat-plate boundary layer

LES and DNS is presented first. This is followed by a discussion and a review of solid–solid and solid–rigid-lid junctures, and a brief discussion on turbulence–free-surface interactions.

2.1. Turbulent flat-plate boundary layer

Very few investigators (Rai and Moin [4], Rai *et al.* [6]) have attempted DNS/LES of spatially developing turbulent flat-plate boundary layer flows. These studies showed the feasibility of performing spatially developing transitional-turbulent boundary layer flows, even though computationally very intensive. Other investigators [7–10] have obtained results similar to a spatially developing flat-plate boundary layer using various approximations to recycle the exiting turbulence back into the computational domain. Other numerical investigations to date have used fully periodic boundary conditions in the streamwise direction. Even though such an assumption is truly justified only for fully developed flows, e.g. channel or duct flows, temporal simulations are useful in studying spatially developing flows, e.g. mixing layers and flat-plate boundary layers [11–13]. Like other LES and DNS studies, most of the earlier simulations were performed using spectral methods; whereas the recent simulations are mainly performed using finite difference techniques with the order of accuracy ranging from second-order to fourth- or even higher-orders. Apart from the differences in numerical schemes, the above mentioned simulations differ from each other with regard to the grid resolutions, subgrid-scale models in the case of LES studies and the overall quality of the results obtained. While some of the studies have been able to reproduce the important quantitative features of the flat-plate boundary layer flows, others obtained on coarser grids were focusing primarily on the qualitative aspects of the flow field. Since the focus of the present work is on juncture flows, a detailed evaluation of the relative merits and demerits of each of the above simulations is not attempted here.

The objectives of the boundary layer simulations reported in this study are to ensure a credible and satisfactory initial condition for the juncture flow simulations and to serve as a validation test for the present implementation of the numerical scheme and the assumptions made.

2.2. Turbulent juncture flows

Turbulent flows in streamwise corners are characterized by the presence of secondary flows of the second kind which are generally understood to be driven by gradients in Reynolds stress distributions [14,15]. These secondary flows appear as streamwise vortices at the junction of two interacting boundary layers. Such vortices are observed experimentally in channel and duct flows, where boundary layers of the side walls meet the top free-surface/wall or the bottom wall.

2.2.1. Solid–solid juncture flows. There are quite a few numerical simulations and experimental investigations of secondary flows in solid–solid corner flows in the literature. Most of the numerical simulations and experimental measurements are for fully developed channel flows or straight duct flows. Here, some of the LES work that has been done examining this problem is reviewed. Miyake and Kajishima [16] performed a LES to study the secondary flow fields in square straight ducts. Madabhushi and Vanka [17] also performed a similar simulation and obtained only qualitative comparisons with experimentally measured quantities. The deviations from the experiments were attributed to the mismatch in Reynolds numbers. Recently, Su and Friedrich [18] performed a LES of the same problem on a range of grids and obtained excellent comparisons with experiments for mean and turbulent quantities. The SGS model used in their study was a modified version of the model developed by Schumann [19].

While all the previous numerical investigations are for fully developed channel flows, Kornilov and Kharitonov [5] conducted an experimental investigation of developing solid–solid juncture flows. They studied the interaction of developing boundary layers of differing thicknesses and found that the flow structure, especially the formation of secondary vortices, is to a large extent dependent on the magnitude of the asymmetry parameter (Γ). Here, Γ is defined as the ratio of thicknesses of the interacting boundary layers. Their findings and results will be revisited several times in this paper in later sections.

2.2.2. Solid–rigid-lid juncture flows. As mentioned earlier, rigid-lid boundary conditions are often quoted in the literature as a representation of a non-deforming free-surface for incompressible flows. They are also used in place of inviscid walls (slip walls). For free-surface flows, the exact boundary treatment demands the satisfaction of the kinematic and dynamic conditions. Historically, investigators have used different levels of approximations and assumptions for the sake of simplicity. The above mentioned rigid-lid assumption is at the lowest level of generality, wherein the free-surface is assumed to be fixed and flat. Under this assumption, the velocity component normal to the free-surface vanishes due to the kinematic constraint. Zero derivative conditions are applied on the other two velocity components. The application of a rigid-lid boundary can be seen in [20–22]. At the next level of generality is the linearized free-surface boundary condition as applied by Mangiavacchi *et al.* [23] and Komori *et al.* [24]. After the linearized free-surface boundary conditions, comes the exact treatment where the free surface is allowed to deform and all the kinematic and dynamical conditions are identically satisfied. However, as noted earlier, a rigid-lid type boundary is applied in the present work.

In numerical investigations to date, where turbulence-driven secondary flows in solid–rigid-lid junctures are studied, the outer flow is fully developed, e.g. the fully developed open channel flow [25]. Leighton *et al.* [26] conducted a DNS of a solid–rigid-lid juncture flow starting with a fully developed channel flow DNS data as an initial condition. The numerical and the accompanying experimental investigation [27] indicate the presence of a counter-clockwise streamwise oriented vortex in the inner region of the juncture, driving the flow at the free-surface towards the wall. In the outer region, the flow is up towards the free surface and out away from the wall which thickens the boundary layer near the free-surface. Apart from these studies, there are two other experimental studies, namely [3,28]. While the measurements of Logory *et al.* [28] are taken in wake of surface-piercing flat-plate, the measurements of Longo *et al.* [3] are for both boundary layer and wake. As noted earlier, the data of Longo *et al.* represents the most complete in terms of mean flow quantities, Reynolds stresses and a detailed uncertainty analysis. Longo *et al.* also observed a counter-clockwise streamwise oriented vortex near the juncture and an outer region of high streamwise vortcity of the opposite sense. Their findings will be discussed further in later sections when comparisons are made with the present numerical investigation. Before concluding the discussion on solid–free-surface juncture flows, a brief discussion is presented regarding the influence of free-surfaces on underlying turbulence.

There are quite a few numerical and experimental investigations in the literature on the effects of a free-surface boundary on turbulence. A few of the recent ones are given in References [29,30]. One of the commonly observed features is an increase in the turbulent kinetic energy near the free-surface along with an apparent transfer of energy from the surface normal velocity component to the other two components, resulting in a quasi-two-dimensionalization of the turbulence in a layer close to the surface. Previous numerical studies on free-surface turbulence including open channel flows, submerged jets and the evolution of homogeneous turbulence under the influence rigid-lid boundary [21–23,31], have shown similar results. These studies indicate that the intercomponent transfer and the overall increase in kinetic energy near the free surface is due to the anisotropic nature of the dissipation tensor and an overall decrease in dissipation rate near the surface.

3. SOLUTION METHODOLOGY AND COMPUTATIONAL PARAMETERS

A brief introduction to LES is presented along with equations of LES, information on subgrid-scale modeling and the numerical scheme used in this study. This is followed by sections on computational details of the presented simulation, e.g. the reference parameters, computational domain and grid sizes, initial and boundary conditions, and the averaging techniques to obtain mean quantities.

3.1. Large eddy simulation

The basis of LES is that only small scales that tend to be isotropic and hence more universal in nature, need be modeled, while the energy carrying large scale eddies are computed. The resolved large scales in LES are defined with respect to a filter function that filters out the small scales. Henceforth, this filter will be referred to as the primary filter. Furthermore, the small scales carry a small portion of the total turbulent energy, and thus one anticipates that the SGS models are less complex than those required for the Reynolds-averaged (RANS) equations. The most widely used SGS model is the eddy viscosity model based on the Smagorinsky formula [32].

3.2. Equations of large eddy simulations

The Navier–Stokes equations are Favre-filtered. Let a tilde ($\sim$) denote a Favre-filtered quantity and an overbar ($-$) denote the space-filtering operation. Following Erlebacher *et al.* [33], we introduce the Favre-filtered field,

$$\tilde{f} = \frac{\overline{\rho f}}{\bar{\rho}}, \tag{1}$$

and decompose the total flow field into a resolvable field $\tilde{f}$ and a subgrid-scale field f',

$$f = \tilde{f} + f'. \tag{2}$$

Filtering the mass and momentum equations, we obtain

$$\frac{\partial \bar{\rho}}{\partial t} + \frac{\partial(\bar{\rho}\tilde{u}_j)}{\partial x_j} = 0 \tag{3}$$

$$\frac{\partial \bar{\rho}\tilde{u}_i}{\partial t} + \frac{\partial}{\partial x_j}[\bar{\rho}\tilde{u}_i\tilde{u}_j + \bar{p}\delta_{ij} + R_{ij} - \bar{\tau}_{ij}] = 0, \tag{4}$$

where

$$R_{ij} = \bar{\rho}(\widetilde{u_i u_j} - \tilde{u}_i\tilde{u}_j) \tag{5}$$

is the subgrid-stress tensor and $\bar{\tau}_{ij}$ is the viscous stress tensor. The filtered pressure is given by

$$\bar{p} = \bar{\rho}R\tilde{T}, \tag{6}$$

where $\tilde{T}$ is the resolvable temperature field and R is the gas constant.

Filtering the total energy equation, we obtain

$$\frac{\partial(\bar{\rho}\tilde{E}+k)}{\partial t}+\frac{\partial}{\partial x_j}\left[(\bar{\rho}\tilde{E}+\bar{p})\tilde{u}_j+K_j+Q_j-\overline{u_i\tau_{ji}}+\bar{q}_j\right]=0, \tag{7}$$

where

$$\tilde{E}=\tilde{e}+\frac{1}{2}\tilde{u}_i\tilde{u}_i, \tag{8}$$

$$Q_j=C_p\bar{\rho}(\tilde{T}u_j-\tilde{T}\tilde{u}_j), \tag{9}$$

$$k=\frac{1}{2}(R_{ii}), \tag{10}$$

$$K_j=\frac{1}{2}\bar{\rho}(\tilde{u}_i\tilde{\tilde{u}}_i\tilde{u}_j-\tilde{u}_i\tilde{u}_i\tilde{u}_j). \tag{11}$$

More details of the equations can be found in Reference [34].

3.3. Subgrid-scale model

The subgrid-scale eddy viscosity used is this study is the compressible version of the Smagorinsky formula due to Erlebacher *et al.* [33]. The model constant is computed using the dynamic modeling procedure in [1]. Central to this dynamic modeling technique is the application of a test filter with a larger filter-width than the primary filter. In the present implementation, the test filtering is performed using a box filter in the physical space. A key input to the calculation of the model constant is the ratio of the test filter to the primary filter. This ratio is usually referred to in the literature as α. In the dynamic model calculations, it is common practice to compute the product $C_R\Delta^2$ rather than model constant C_R independently, and the only filter parameter that needs to be specified is α. Here Δ^2 is the width of the primary filter. In the present investigation, the value of α is taken as 2. A complete discussion on the model including the derivation of the model constants and details of the present implementation of the box filter is provided in [34,35], thus not repeated here.

An averaging procedure is usually adopted to make the constants well conditioned. These averages are generally taken along a direction in which the turbulence is assumed to be homogeneous. Thus, the constants obtained are independent of the directions in which turbulence is homogeneous. There are some mathematical inconsistencies associated with treating C_R as a constant in the averaging operation. Akselvoll and Moin [36] rectified these inconsistencies in their dynamic localization technique and found that the inconsistencies due to the averaging process have only minimal effects on the results for the flow over a backward facing step. The details of the dynamic localization technique is given in [37]. In addition to overcoming the mathematical inconsistencies inherent in the averaging procedure, the dynamic localization technique has a major advantage in that it can be applied to more general flows which may not possess any homogeneous directions. However, localization modeling is yet to gain widespread usage by the LES research community. The present implementation of the model also does not make use of the dynamic localization technique.

3.4. Numerical scheme

The numerical scheme used in this study is a modified MacCormack scheme developed by Gottlieb and Turkel [38]. The scheme is explicit second-order-accurate in time, and fourth-order in space for the convective terms and second-order for the viscous terms. This scheme has been previously used for temporally developing transitional-turbulent flat-plate boundary layer flows [12,13]. Sreedhar [34] and Ragab *et al.* [39] used this scheme for LES of turbulent vortices and mixing layers. Implementation of the scheme for temporal simulations and code validation using linear stability analysis results are given in [34,35].

3.5. Computational parameters

The reference length, δ, is the quantity $\sqrt{vx/U_0}$, and the reference velocity, U_0, is the free stream velocity. Here v is the kinematic viscosity and x is the co-ordinate along the plate. The Reynolds number based on δ is 600 and those based on initial displacement thickness (δ_1) and momentum thickness (δ_2) are about 1000 and 400 respectively. The Mach number based on the free stream velocity and speed of sound in the far field is 0.4. At this level, the flow is sufficiently incompressible without making the equations excessively stiff.

3.5.1. Computational domain and grids. The computational box is of dimensions $L_x = (2\pi/\alpha)\delta$ in the streamwise direction, $L_y = 40\delta$ in the transverse wall-normal direction and $L_z = 20\delta$ in the spanwise direction. Here α is the wavenumber of the linear stability wave which is described in the next section.

Boundary layer simulations were performed on a series of grids, shown in Table I.

In all these simulations, mesh size is uniform in the streamwise (X-) and the spanwise (Z-) directions. It may be noted that the spanwise grid spacing used in this study for all the grids is very conservative for 2D canonical flat-plate boundary layers. The grid in the transverse direction is stretched to cluster points inside the boundary layer. While the near-wall mesh spacing of the finest grids (grids D and E) is sufficient to resolve the wall layer, the near-wall spacings on the three coarser grids (A, B and C) may not be sufficient to fully resolve the wall layer accurately. The grids C and D are only mildly stretched in the transverse direction compared with the other grids, resulting in more points in the logarithmic region. The mild stretching in the transverse direction and the relatively low spanwise spacings help keep the aspect ratio of the grid cells in the YZ-plane to be of the order unity. This is especially true for grid C. While such a feature is unnecessary and not used in practice for 2D canonical boundary layers, it is desirable in the later part of the present investigation, when the same grid is used for the juncture flows, at which time an additional solid-wall or rigid-lid is introduced in the spanwise-normal plane.

Table I. Boundary layer simulations were performed on a series of grids

Grid	Grid size	$y^+_{\min}$	Δz^+	Points in $y^+ < 30$	Points in $30 < y^+ < 300$	Points in $y^+ > 300$
A	$37 \times 33 \times 73$	6.5	6.8	5	15	13
B	$49 \times 33 \times 109$	4.5	4.5	7	13	13
C	$65 \times 49 \times 109$	4.5	4.5	7	26	16
D	$97 \times 65 \times 129$	1.8	3.7	18	31	16
E	$72 \times 65 \times 192$	0.9	2.6	20	22	23

3.5.2. Boundary conditions. For the initial flat-plate boundary layer calculations, periodic conditions are imposed in the X- and Z-directions. No-slip along with zero-gradient conditions for temperature and density are used on the plate ($Y=0$). In the far field ($Y=L_y$), zero-gradient boundary conditions are used for all the variables.

For the juncture flow simulations, periodicity in the spanwise direction was relaxed, instead rigid-lid or solid-wall is applied at $Z=0$. The solid–solid juncture flow was obtained by applying a no-slip boundary at $Z=0$ similar to the $Y=0$ boundary. That is

$$\tilde{u}=\tilde{v}=\tilde{w}=0,$$

along with zero-gradient conditions for density and temperature. In the other case, the boundary conditions for velocities at $Z=0$ were chosen to match the rigid-lid approximation which is

$$\tilde{w}=\frac{\partial\tilde{u}}{\partial z}=\frac{\partial\tilde{v}}{\partial z}=0.$$

A zero-gradient condition was applied for density. For temperature, two boundary conditions were tried: a zero-gradient condition and a fixed temperature condition based on the free stream parameters. An examination of the results obtained showed no significant change in the results due to the treatment of the temperature boundary condition. The modified boundary at the far field $Z=L_z$ is treated the same way as the far field boundary in the transverse ($Y=L_y$) direction.

The computational domain and the boundary conditions are shown in Figure 1

3.5.3. Initial conditions. For generating the turbulent flow-field on the flat-plate, the initial field consists of compressible Blasius solutions with superimposed perturbations. Perturbations consist of 2D linear stability waves and random noise. The streamwise wavenumber (α) of the disturbance is 0.14. Thus, the initial condition for any generic variable u may be represented as

$$u(x,y,z)=a_{2d}u_{\alpha 2d}(\alpha,x,y)+a_{3d}f(y)R(x,y,z). \tag{12}$$

Here $u_{\alpha 2d}$ is the linear stability eigenwave and a_{2d} is its amplitude. In the present investigation, the maximum amplitude of the eigenwave is initialized to be 2% of the mean streamwise velocity. The $R(x,y,z)$ in the above expression represents a random number generated by the computer in the range -1 to $+1$. The function f is chosen such that it assumes low values very near the plate and outside the boundary layer in the free stream. The magnitude of the 3D disturbance, a_{3d}, is taken to be $<1\%$ of the mean streamwise velocity.

Forcing functions [12,13] are added to the right-hand side of the x-momentum and the energy equation to prevent the mean flow profile from degenerating into an error function profile.

The turbulent flow-field generated on a flat-plate is used as an initial condition to study the juncture flow. The procedure of modifying the boundary conditions after an initial flow-field has been generated has been previously adopted [26,31,40]. Biringen and Reynolds [40] and Walker *et al.* [31] used a homogeneous turbulent flow-field as their initial condition and then applied a no slip and a shear-free boundary condition on two boundaries to study the characteristics of shear-free turbulent boundary layers using LES. Leighton *et al.* [26] obtained fully developed channel flow simulation data and then modified the boundary conditions to study the turbulent flow-field in a corner configuration. A similar technique is followed in the present investigation where the turbulent boundary layer simulation data serves as the initial condition for the juncture flow simulations with modified boundary conditions.

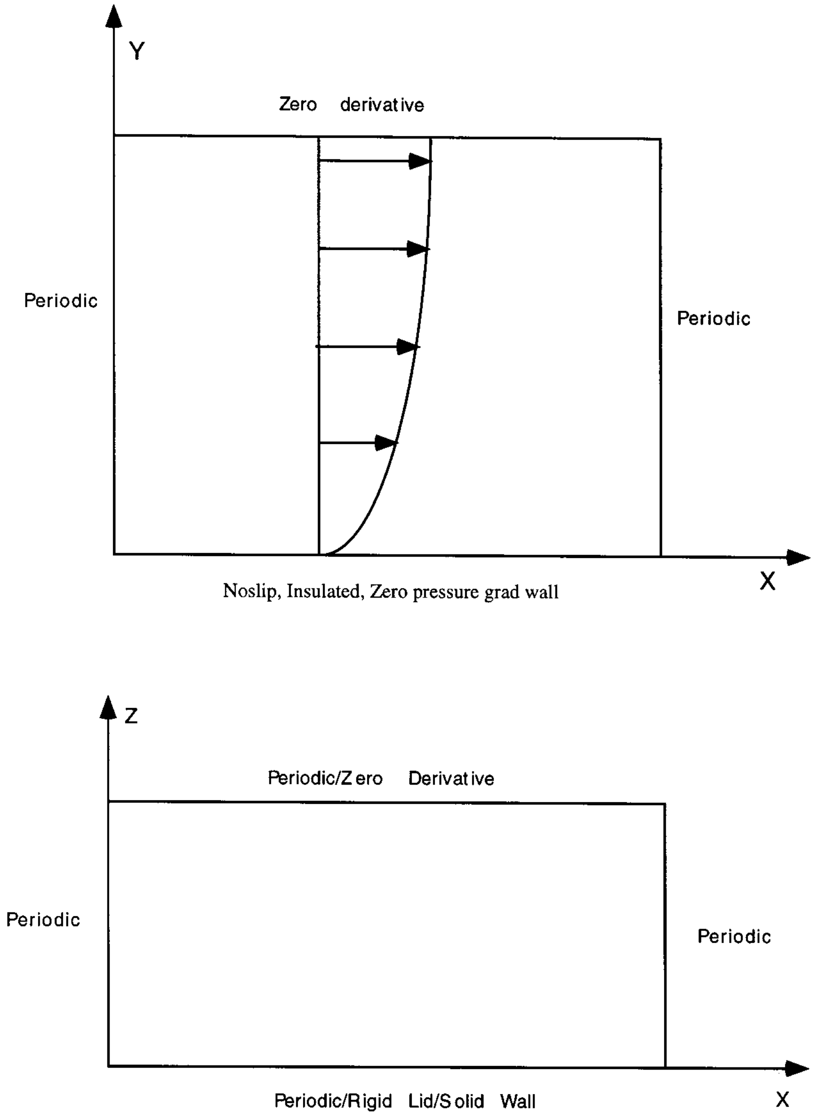

Figure 1. Computational domain and boundary conditions.

3.5.4. Mean flow quantities. Mean flow quantities were obtained for the boundary layer calculations by spatial averaging in the two homogeneous periodic directions. For the juncture flows, the spanwise direction is no longer homogeneous, which means one less direction for averaging. For improving the statistical quantities, one could either perform a time averaging or an ensemble averaging. For statistically steady flows such as a fully developed channel flow, the mean quantities from a temporal simulation are usually obtained by averaging in time. However, for developing flow-fields like the ones considered in this study, such an averaging would be unjustified for temporal simulations. Instead, an ensemble averaging was performed. Simulations were repeated on a single grid starting with different initial levels of perturbations. While the maximum amplitude of the linear stability wave was kept at 2% of the mean flow, the root mean square values of the random fluctuations were varied from 1% to 1/10% of the mean flow from one simulation to another. Also the distribution [$f(y)$ in Equation (12)] of the random noise in the domain was varied from one simulation to another.

4. RESULTS

Results are presented for the turbulent boundary layer calculations and validated by comparisons with experimental and DNS data. The juncture flow simulations are presented next, with results evaluated with respect to experimental data. The issues discussed include the formation of secondary vortices, the role of the anisotropy of normal Reynolds stresses and the significance of the asymmetry parameter on the generation of the vortices.

4.1. Turbulent boundary layer

Some representative results of the transitional boundary layer are presented first, followed by the results of the fully turbulent boundary layer. The fully turbulent boundary layer results are validated with regards to mean velocity and Reynolds stresses.

Starting from the initial laminar profile, the disturbances were allowed to grow in time. Transition to turbulence begins at a non-dimensional time of about 750 as seen in Figure 2, which shows the evolution of displacement thickness (δ_1), the shape factor (H) and skin friction coefficient (C_f). These curves are shown for grid C. Here H is the defined as the ratio of the displacement thickness to the momentum thickness (δ_2). The shape factor has an initial value of 2.6, which is the laminar value for incompressible flow. During the transition period it drops to 1.45, which is very close to the value for incompressible turbulent flow. Once the flow is fully turbulent, it stays very close to the turbulent value. The displacement thickness also shows a higher growth rate after the beginning of transition. The sharp jump in the skin

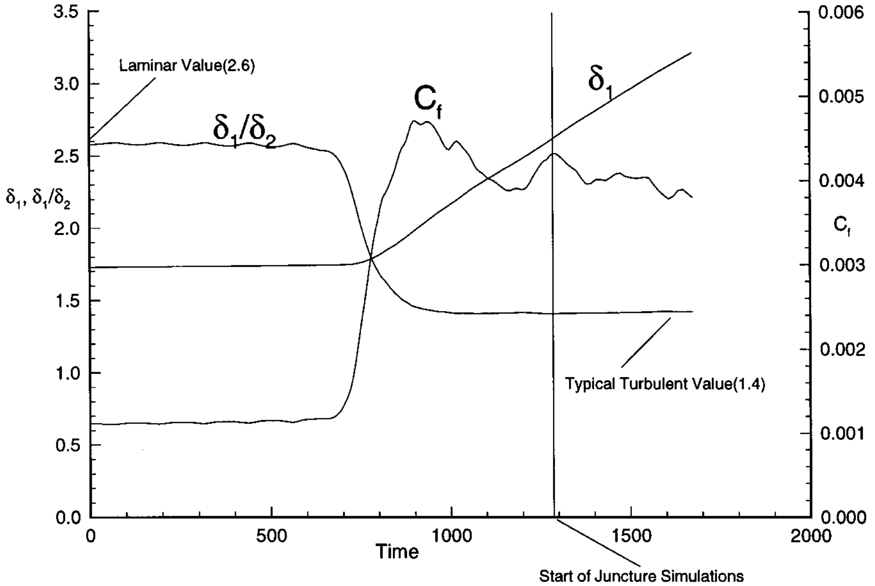

Figure 2. Evolution of displacement thickness, shape factor and skin friction for the boundary layer.

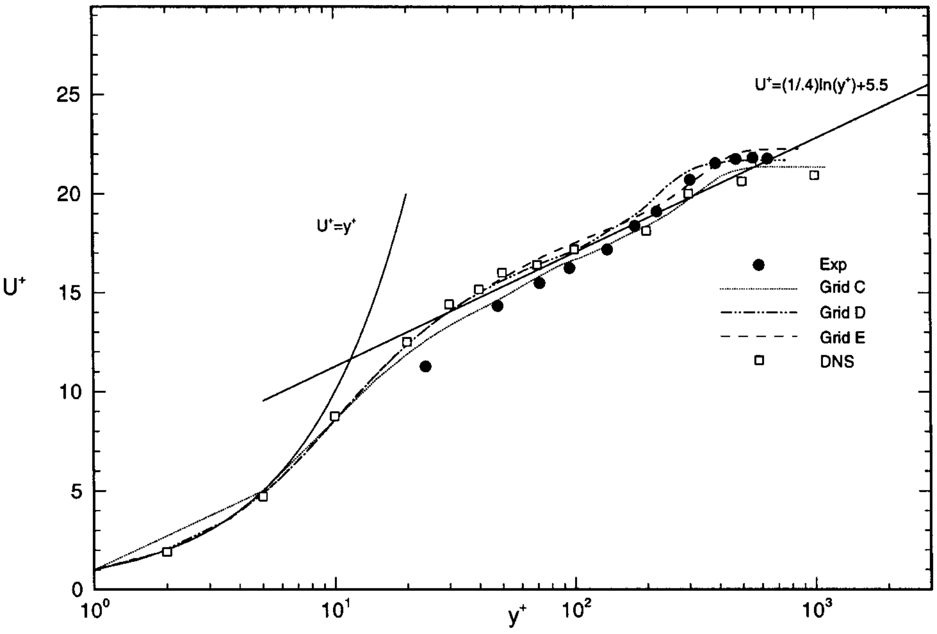

Figure 3. Mean streamwise velocity profile, experimental data ([3], $Re_\theta = 1160$) and DNS ([4], $Re_\theta = 1350$). Computations are at $Re_\theta = 1150$.

friction coefficient (C_f) within a short period of time is typical of the transition process. Here C_f is defined as $2\tau_{\mathrm{wall}}/\rho U_0^2$ where τ_{wall} is the friction at the wall. Later, the skin friction settles down to a lower value of about 3.98. Comparisons with experiments are made when the Reynolds number, based on the momentum thickness, is about 1150; at which point the non-dimensional time is about 1250. The corresponding experimentally measured values at this Reynolds number for a flat-plate boundary layer are: $H = 1.48$ and $C_f = 4.00$. Even on the coarsest grid (grid A) with the wall layer not resolved, qualitative features such as the sudden jump in the skin friction and the reduction in the shape factor were observable. However, the results obtained on the coarser grids did not compare well with the experimental and DNS data with regard to mean velocity and stresses. Hence, the following validation is shown only for the three finer grids.

The mean streamwise velocity is shown first. The U^+ is plotted against the y^+ coordinates. Figure 3 shows the computed profile along with the experimentally measured and DNS profiles. The curves corresponding to grids D and E are almost identical with a well discernible logarithmic region. In the outer region, however, there are differences. This is due to the different stretching functions used in grids D and E for the same number of points in the transverse direction. Even though grid C shows differences in comparison with the two finer grids, it generally follows the correct trend.

Figure 4 shows the comparison of turbulent intensities with the experimental and DNS data. All the turbulence intensities are scaled with the friction velocity ($u_\tau = \sqrt{\tau_{\mathrm{wall}}/\rho U_0^2}$). The root mean square quantities are in satisfactory agreement with the experimental and DNS data. The grid E results are closer to the DNS data, especially for the streamwise component. The peak value is underpredicted by grids C and D, especially for the streamwise and spanwise components. In spite of these differences, the results obtained on grids C and D show the correct trends. The difference between DNS and the present simulations are greatest for values of $y^+ > 500$. Rai and Moin attributes the high edge values of turbulence intensities in their simulation to the free-stream turbulence levels.

From the results presented, it is clear that a temporally developing LES is capable of capturing most of the pertinent features of the transitional-turbulent flat-plate boundary layer flow. The satisfactory comparison with the experimental and DNS data on different grids is a validation of the present implementation of the numerical scheme.

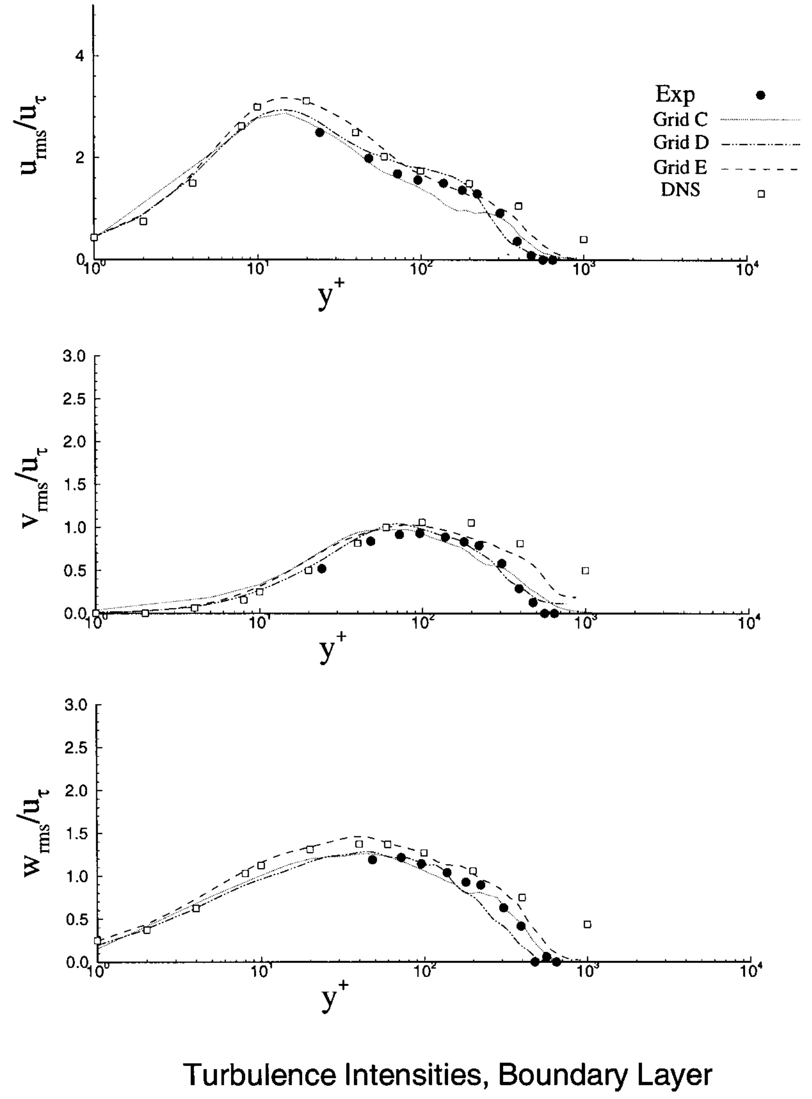

Turbulence Intensities, Boundary Layer

Figure 4. Normal Reynolds stresses, experimental data ([3]; $Re_\theta = 1160$) and DNS ([4], $Re_\theta = 1350$). Computations are at $Re_\theta = 1150$.

4.2. *Juncture flow simulations*

As described earlier, the juncture flow simulations are initialized with the boundary layer simulation results but with modified boundary conditions at $Z = 0$. The averaging for statistical quantities were performed in the streamwise direction along with an ensemble averaging over different realizations. Grid C was selected for this purpose. The justifications for selecting grid C are

(1) Satisfactory turbulent boundary layer results were obtained on grid C, including the normal Reynolds stresses, which play a crucial role in the generation of turbulence-induced secondary flows.

(2) On grid C, the stretching in the Y-direction is very mild and all the grid cells in the juncture region have aspect ratios close to unity. This is a very desirable feature for the juncture flow where weak secondary flows are generated.

(3) Computational requirements for the finer grids, especially in view of the additional runs required for ensemble averaging for the juncture flows, are extremely high.

To facilitate ensemble averaging, four simulations were performed on grid C, varying the distribution of the initial perturbation as described in an earlier section. These different initial conditions did not show any significant effect on the time of onset of transition. The streamwise-averaged mean flow quantities also showed no significant deviations from each other even though the instantaneous flow structures showed variations. While an ensemble of four is a small sample size, it should be recalled that this is in addition to the averaging done in the homogeneous streamwise direction. Thus the averaged quantities obtained are functions of Y and Z for the juncture flow; as opposed to functions of Y only for the 2D canonical boundary layer. As a further check, one realization of the juncture flow simulations was performed on each of the grids B and D to see the dependence of the results on the grid. The mean flow structures obtained by spatial averaging alone in the streamwise direction were found to be rough in comparison with the ensemble averaged ones.

The simulation with the modified boundary conditions was started at a non-dimensional time of about $T = 1300$ and continued until $T = 1675$. As a final case, we continued the simulation, leaving the spanwise periodic boundary conditions untouched, which is essentially a pure temporally developing boundary layer flow, for the same time interval as the other two cases.

In the following, responses of the turbulent flow-field to these different boundary conditions and how each of these boundary conditions affected large-scale flow patterns in the corner region, are discussed.

4.3. *Comparison of the flow-fields*

In this section, we compare the pure boundary layer (PBL), the solid–solid corner (SSC) and the solid–rigid-lid corner (SRL). The contours of the mean streamwise velocity in the YZ-plane are shown in Figure 5. No significant variation in the spanwise direction is seen for the PBL; whereas for the SSC and SRL, the effect of the modified boundary at $Z = 0$ is obvious. For the SSC, a thin boundary layer is seen developing on the $Z = 0$ wall in comparison with the $Y = 0$ wall. For the SRL, the boundary layer near the rigid-lid boundary has thickened compared with the $Z = L_z$ boundary. Similar behavior is reported by Longo *et al.*

Contours of the cross-plane (Y-Z) components of mean velocity (not shown here) also showed a clear influence of the no-slip and the rigid-lid boundaries on the flow-field. The transverse velocity has high positive values near the rigid-lid boundary in the outer part of the

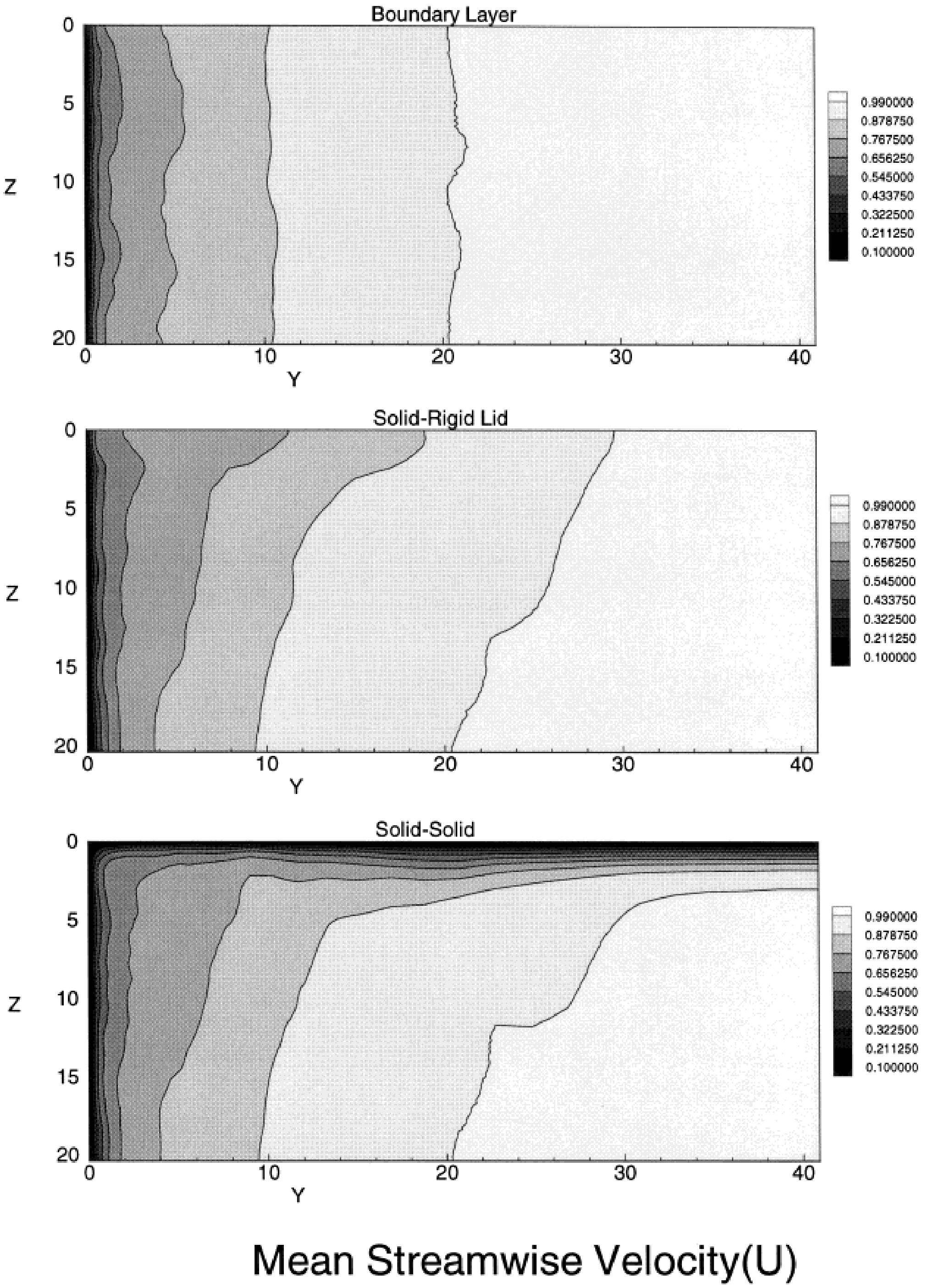

Figure 5. Contours of mean streamwise velocity (U) in the YZ-plane for the three cases. From top, PBL, solid–rigid-lid juncture and solid–solid juncture.

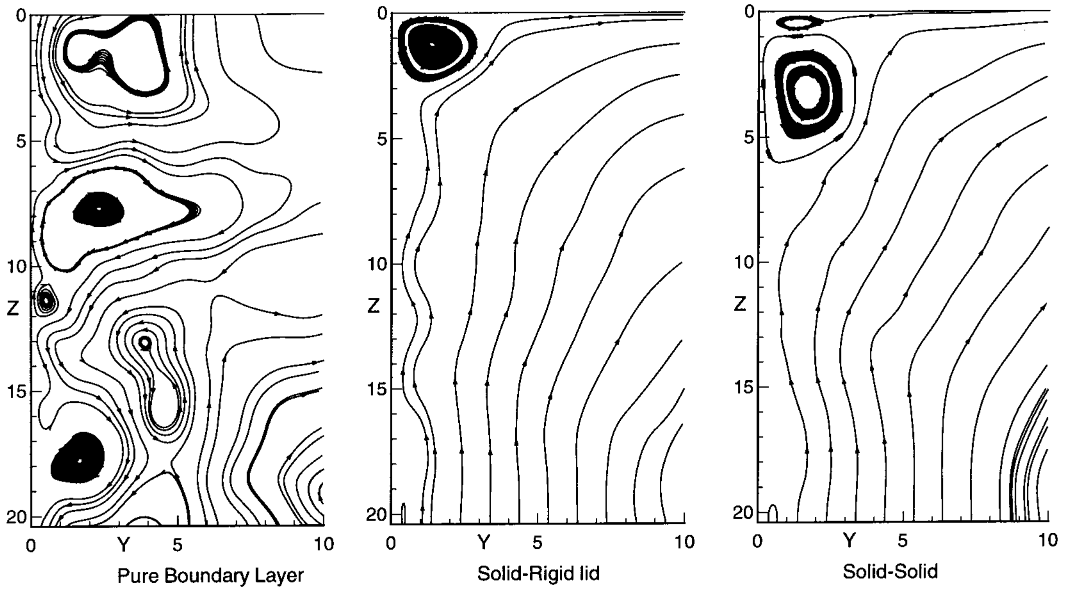

Figure 6. Streamtraces in the *YZ*-plane for the three cases. From left to right, PBL, solid–rigid-lid juncture and solid–solid juncture.

boundary layer which causes the boundary layer to thicken. However, very close to the juncture, contours indicate that the flow at the rigid-lid boundary are directed towards the wall. A similar finding is reported in Reference [26] near a SRL in their DNS study of a fully developed juncture flow. More comparisons and details of the above DNS study are given in next section.

The overall behavior of mean velocity components in the cross-plane are similar for SSC and SRL, except for the differences in the vicinity of the juncture and the regions very close to the $Z = 0$ boundary where no-slip conditions are applied for SSC. This can be more clearly seen from the streamlines in the cross-plane which are shown and discussed in the next section.

4.3.1. Secondary corner vortices. To investigate the formation of turbulence-driven secondary vortices in the streamwise corner, the mean velocity vectors in the *Y*-*Z* plane were looked at. Shown in Figure 6 are streamlines obtained from the mean velocity vectors in the cross plane. While many random structures can be seen for the PBL, a counter-clockwise vortex in the corner can be seen for the SSC and SRL. These large vortices appear to be the most dominating feature of the two corner flows under consideration. An additional smaller vortex is present near the $Z = 0$ boundary for the SSC. Typically, the turbulent flow-field in a flat-plate boundary layer contains streamwise-oriented vortices close to the wall. Since the streamwise extent of these vortices can be sufficiently large, averaging in streamwise direction alone does not necessarily remove these vortices. However, averaging over a large number of ensembles should weaken or average out these vortices. The persistence and the apparent strengthening of the corner vortices, even after ensemble averaging, is an indication that these vortices are truly due to the influence of the boundary conditions at $Z = 0$ rather than a randomly generated vortex in a turbulent flow. Similar corner vortices were obtained in the simulation obtained using grids B and D, showing that these results are grid independent.

The relative size and location of the two vortices in the SSC are in qualitative agreement with the experimental observations of Kornilov and Kharitonov [5]. Due to the unavailability of detailed data from their experimental measurements, the size of these vortices are roughly estimated (from Figure 4 in Reference [5]) to be about a third of the boundary layer thickness. Unlike the SSC, only one vortex is seen near the rigid-lid boundary in SRL. This is in contrast to the data of Longo *et al.*, where two distinct regions of vortical motions of the opposite sense were observed: a counter-clockwise vortex motion in the inner part and a region of opposite sign vorticity in the outer part of boundary layer. The DNS results of Leighton *et al.* also indicated only one counter-clockwise vortex in the juncture region in the solid–rigid-lid corner flow. However, it should be noted that the computational domain and set up of the DNS of Leighton *et al.* does not exactly correspond to the present LES or the experiments of Longo *et al.* Their initial conditions were obtained from a fully developed channel flow and the extent of their domain in the wall normal direction was only up to y^+ of about 300.

In order to explain and understand the absence of the outer vortical region, the governing equation for the mean streamwise vorticity will be looked at.

4.3.2. Mean streamwise vorticity and anisotropy of normal stresses. The genesis of the turbulence-driven secondary vortices is generally understood to be due to the anisotropy of the turbulence and to the gradients in the normal turbulent stresses. The equation governing the evolution of mean streamwise vorticity, ξ, for incompressible turbulent flows is given below. The entire equation is given for the sake of completeness.

$$\begin{aligned}&\left(U\frac{\partial\xi}{\partial x}+V\frac{\partial\xi}{\partial y}+W\frac{\partial\xi}{\partial z}\right)\\&=\left(\xi\frac{\partial U}{\partial x}+\eta\frac{\partial V}{\partial y}+\zeta\frac{\partial W}{\partial z}\right)+\frac{1}{Re}\left(\frac{\partial^2\xi}{\partial x^2}+\frac{\partial^2\xi}{\partial y^2}+\frac{\partial^2\xi}{\partial z^2}\right)+\frac{\partial}{\partial x}\left(\frac{\partial\overline{u'v'}}{\partial z}-\frac{\partial\overline{u'w'}}{\partial y}\right)\\&\quad+\frac{\partial^2}{\partial y\,\partial z}(\overline{v'v'}-\overline{w'w'})+\left(\frac{\partial^2}{\partial z^2}-\frac{\partial^2}{\partial y^2}\right)\overline{v'w'}.\end{aligned}\tag{13}$$

Based on experimental and theoretical observations, it has been previously argued by many investigators that the second last term on the right-hand side which contains $(\overline{v'v'}-\overline{w'w'})$, is primarily responsible for the generation of these vortices for fully developed flows (see [14]). Whereas the last term which contains the $\overline{v'w'}$ is known to have a damping effect; the term $(\overline{v'v'}-\overline{w'w'})$ is a measure of the anisotropy of the normal Reynolds stresses in the YZ-plane. In Figure 7 the contours of the anisotropy term $(\overline{v'v'}-\overline{w'w'})$ in the YZ-plane are shown . For the PBL, the contour levels are all negative which is a key feature of near-wall flows where the spanwise component of the velocity fluctuations are larger than the transverse (wall normal) velocity fluctuations. This is also true for free-surface flows where the surface normal component of velocity fluctuations are suppressed. In a juncture configuration, two such regions of opposite signs merge; this gives rise to gradients in the anisotropy term. This is clear from the distribution of the anisotropy terms in the SSC and SRL that show high positive values near the $Z=0$ boundary and predominantly negative values near the $Y=0$ boundary. While the high positive values are concentrated in a much thinner region inside the boundary layer on the $Z=0$ boundary, the negative values are spread out over the thicker boundary layer region on the $Y=0$ boundary. The extreme values, which are predominantly near the boundaries, drop to near-zero values away from the boundaries as the two regions merge. The zero contour line can then be defined as a line that divides the corner into two with the higher angle on the thicker boundary layer side.

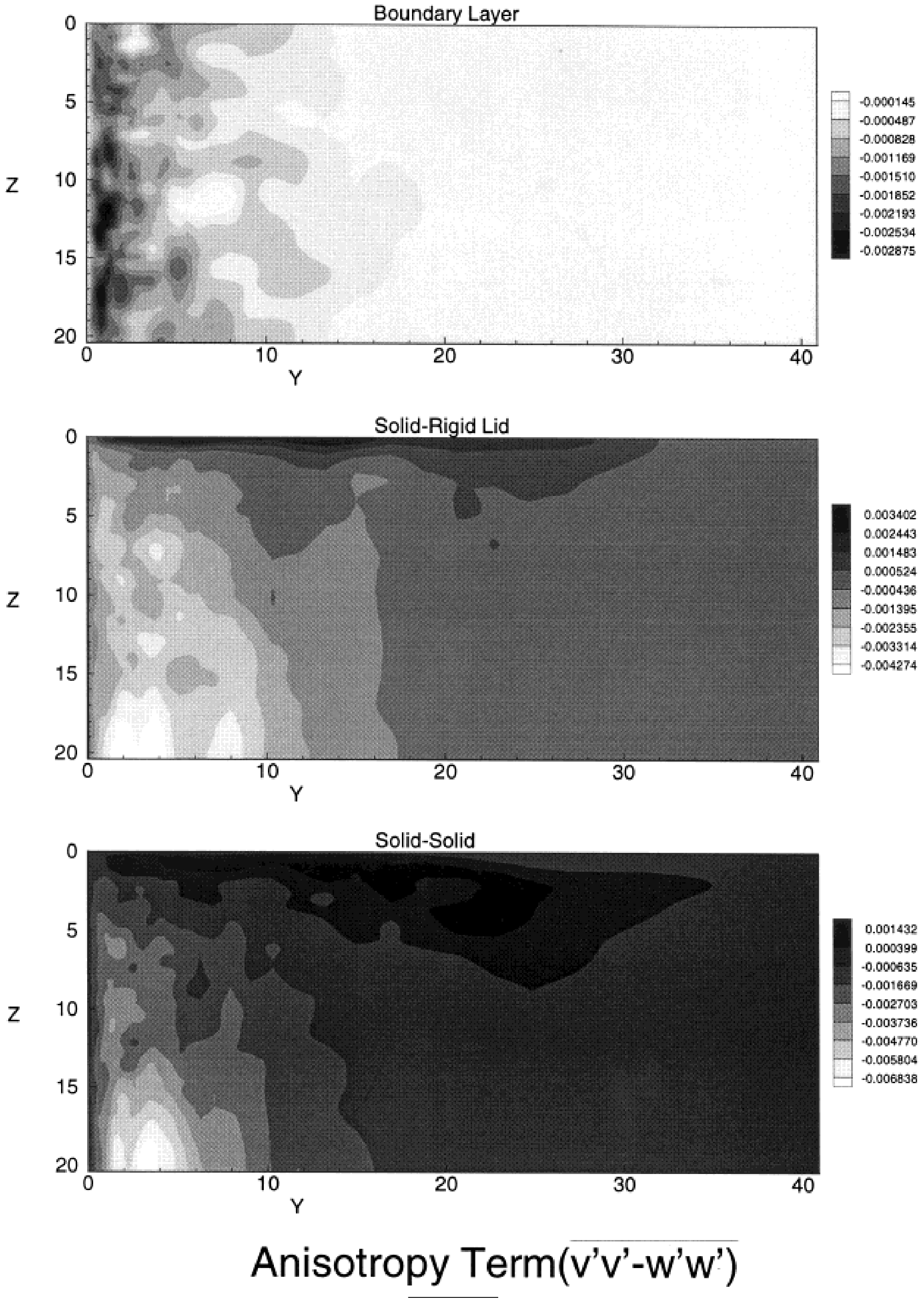

Figure 7. Contours of the mean anisotropy term ($\overline{v'v' - w'w'}$) for the three cases. From top, PBL, solid–rigid-lid juncture and solid–solid juncture.

In Figure 8 the variation of the anisotropy term $(\overline{v'v'} - \overline{w'w'})$ is shown along the Y- and Z-direction at various Z and Y locations, respectively. In this figure, the distances are normalized by the distance from the axes to the zero contour line while the anisotropy term is normalized by the maximum value along each such line. Also shown in Figure 8 are the data points from Longo *et al.* and sketches of the approximate locations of the zero contour lines. The results obtained for the SRL display satisfactory qualitative comparisons with the experiments as far as the general shape of the curve is concerned, even though the zero contour lines are off. The variation of $(\overline{v'v'} - \overline{w'w'})$ over the YZ-plane shows similarity. Apart from the solid–free-surface juncture data of Longo *et al.*, the wake flow data in [3], and the open and closed channel flow data in [41] also display the same similarity within the scatter of the data. The behavior of the 2D boundary layer flow also shows similar behavior. This means that the nature of the term $(\overline{v'v'} - \overline{w'w'})$ is such that it depends only on the proximity to the boundary, whether it is a wall (plate) or a free-surface. It may be noted from Figure 8 that the present LES results also showed significant scatter which could be due to the lack of larger sample sizes. Longo *et al.* obtained a curve fit through the similarity curve of the anisotropy term and then reconstructed the second last term in the vorticity equation. It was found that the sign of that term is similar to the sign of the streamwise vorticity (ξ) with blending regions of opposite signs near the zero contour line.

The close resemblance of the pattern of distribution of $(\overline{v'v'} - \overline{w'w'})$ between the SSC and SRL points to the argument that it is the same underlying mechanism that is causing the generation of secondary vortices in the two flow-fields. The only notable difference is the relative size of the regions where the anisotropy term is positive. The relatively larger region for the SSC is due to the thicker boundary layer generated near the $Z = 0$ wall due to the no-slip condition. For a perfectly symmetric corner, where the two boundary layers are of the same thickness (i.e. a corner flow in which the asymmetry parameter Γ is exactly one), we expect the positive and negative values to be symmetrically distributed on either side of the bisector of the corner. This argument can be extended by noting that any increase in Γ will lead to a shrinkage of the positive region near the $Z = 0$ boundary until it reaches the limiting case of the PBL where Γ is infinity.

4.3.3. Significance of asymmetry parameter (Γ). The asymmetry parameter (Γ) is easily computable for solid–solid junctures due to the well defined nature of the boundary layers on no-slip walls. In the present simulation, Γ is estimated to be about 4 towards the end of the simulation for SSC, where Γ is taken as the ratio of the boundary layer thickness on the $Y = 0$ boundary to that of the $Z = 0$ boundary. Following the arguments of the previous section, Γ can also be estimated based on the ratio of the area of the regions where the anisotropy terms are of opposite signs. A similar estimation of Γ yielded a value of about 8 for the SRL and a value of around 2 for solid–free-surface juncture data of Longo *et al.* These values are tabulated in Table II.

Table II.

Investigation	Type of juncture	Γ
Present (SSC)	Solid–solid	4
Kornilov *et al.*	Solid–solid	1–2.3
Present (SRL)	Solid–rigid-lid	8
Longo *et al.*	Solid–free-surface	2

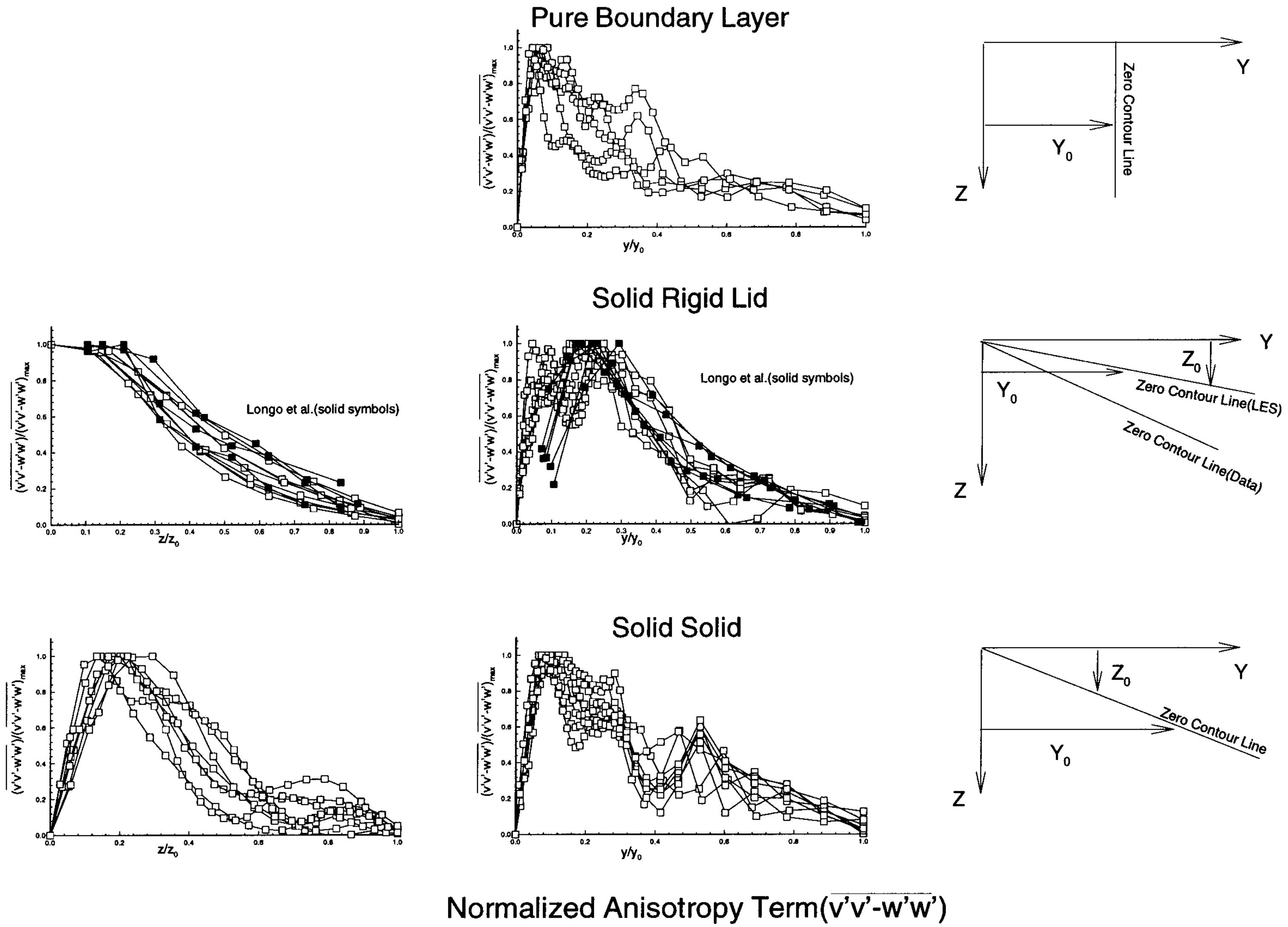

Figure 8. Variation of normalized mean anisotropy term $(\overline{v'v' - w'w'})$ for the boundary layer, solid–rigid-lid and the solid–solid juncture. The solid symbols are the experimental data points of Longo *et al.* [3].

With this information in the backdrop, we come back to take a second look at the secondary flows in the YZ-plane. The smallness of the second vortex for the SSC in the thinner boundary layer region of the corner is attributed to the relatively larger asymmetry parameter. The basis of this conclusion is the experimental findings in [5] which showed that a larger asymmetry parameter resulted in a smaller and much weaker second vortex. Unfortunately, there is not enough data to quantify the relationship between the asymmetry parameter and the relative sizes of the vortices. In their measurements, the largest Γ they considered was 2.3, at which level the vortex in the thinner boundary layer was small. In the present investigation, with Γ for SSC estimated to be around 4, the second vortex is as small as expected. The sign of these vortices are consistent with the findings of Kornilov and Kharitnov.

Extending the above argument for the SRL, the absence of the second vortex may be attributed to the even larger Γ of around eight at which level the second vortex should be extremely small. It should be recalled that the data of Longo *et al.* with Γ about 2, did show a region of very high vorticity near the free-surface, apart from the inner counter-clockwise vortex closer to the solid-wall.

Regarding the size of the vortices, Longo *et al.* estimates the size of the vortical regions to about $0.5\delta_0^2$ where δ_0 is the boundary layer thickness. However, the size of the vortex in the SRL in the present investigation is about $0.1\delta_0^2$.

While the overall prediction of the juncture flow was satisfactory for SSC, the same could not be said about the SRL. This could be due to the inability of the rigid-lid boundary to mimic the true free-surface boundary. Another factor can be the presence of compressibility effects. Moreover, it should be kept in mind that only the boundary conditions are changed in the present study, whereas the governing equations are left untouched. For incompressible free-surface flows, the Froude number appears only in the boundary conditions, where as for compressible flows, the Froude number appears in the momentum and energy equations. These were neglected in the present study. However, the turbulent kinetic energy and individual velocity components showed the correct free-surface limiting behavior near the rigid-lid boundary. This is discussed in the next section.

4.3.4. Turbulent kinetic energy. The effect of these modified boundaries on the turbulent kinetic energy (q) distribution is shown in Figure 9. The kinetic energy increases as the $Z=0$ boundary is approached for the SRL, while it increases and then decreases for the SSC due to presence of the no-slip wall. The variation of the normal stresses and turbulent kinetic energy along the Z-axis at two different Y-locations are shown in Figure 10. For the SSC, the normal stresses and kinetic energy drops to zero near the noslip wall at $Z=0$. The behavior of the kinetic energy and the normal stresses near the $Z=0$ wall are typical of a flat-plate boundary layer. For the SRL, near the rigid-lid boundary, where only the w component of the velocity is made to vanish at the boundary, other two components increase. The departure from the isotropy near the $Z=0$ boundary is very clearly demonstrated by the curves at $Y=0.9\delta$. Away from the $Z=0$ boundary, the normal stresses are isotropic and as they approach the boundary, they branch out. This behavior is in agreement with the previous findings that there is a redistribution of energy from the surface normal velocity component to the other two components near the free-surface. Walker *et al.* [31] attributes the sustenance of the resulting anisotropy in normal Reynolds stresses near a rigid-lid boundary to the reduced dissipation of the tangential velocity fluctuations. It is clear from Figure 10 that the increases in streamwise velocity fluctuations are larger than the spanwise velocity fluctuations. Longo *et al.* also reports the same trend. This is in contrast to the behavior in open channel flows [22] where the increases in spanwise fluctuations are larger than the increases in streamwise fluctuations near the free-surface.

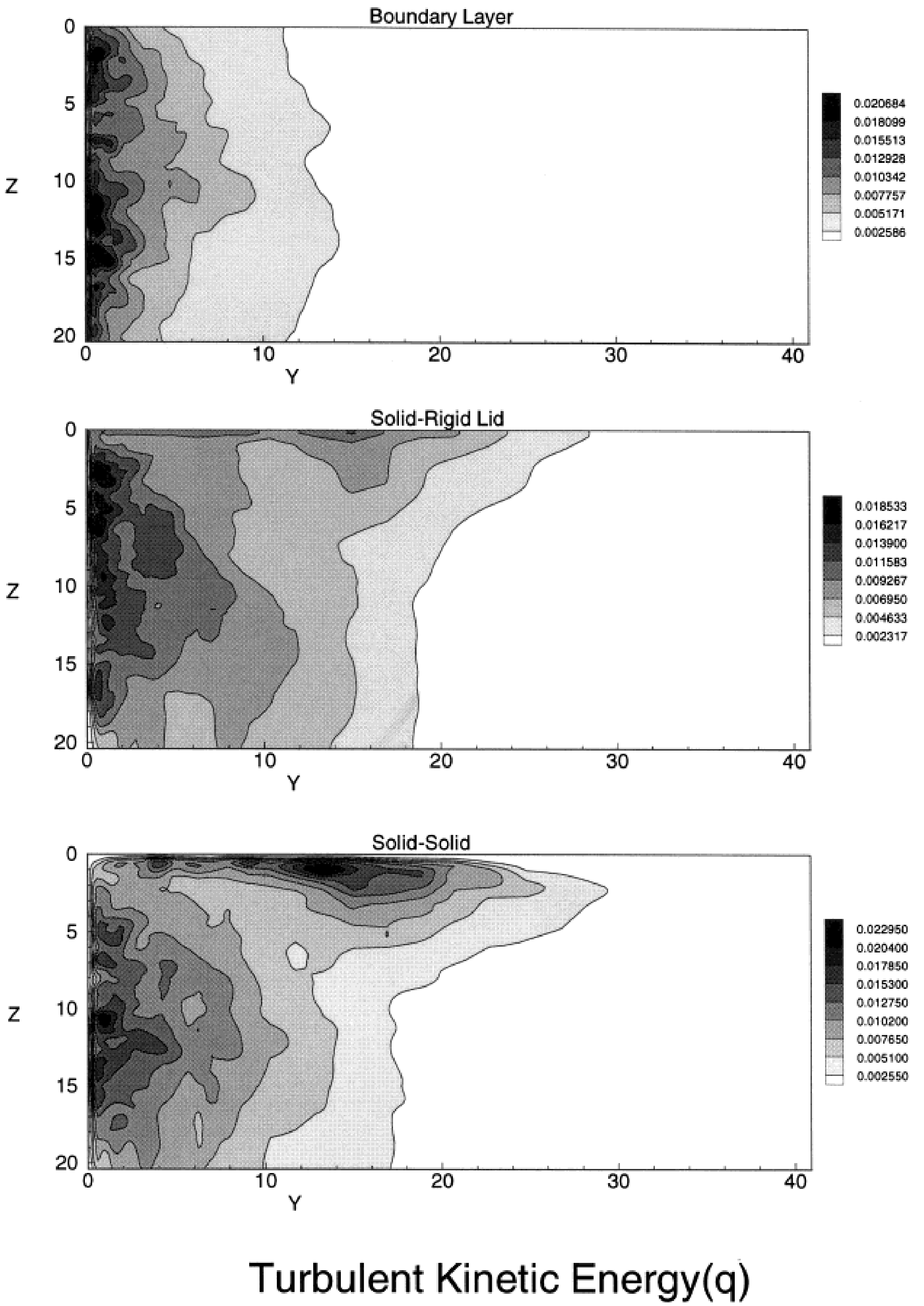

Figure 9. Contours of the turbulent kinetic energy for the three cases. From top, PBL, solid–rigid-lid juncture and solid–solid juncture.

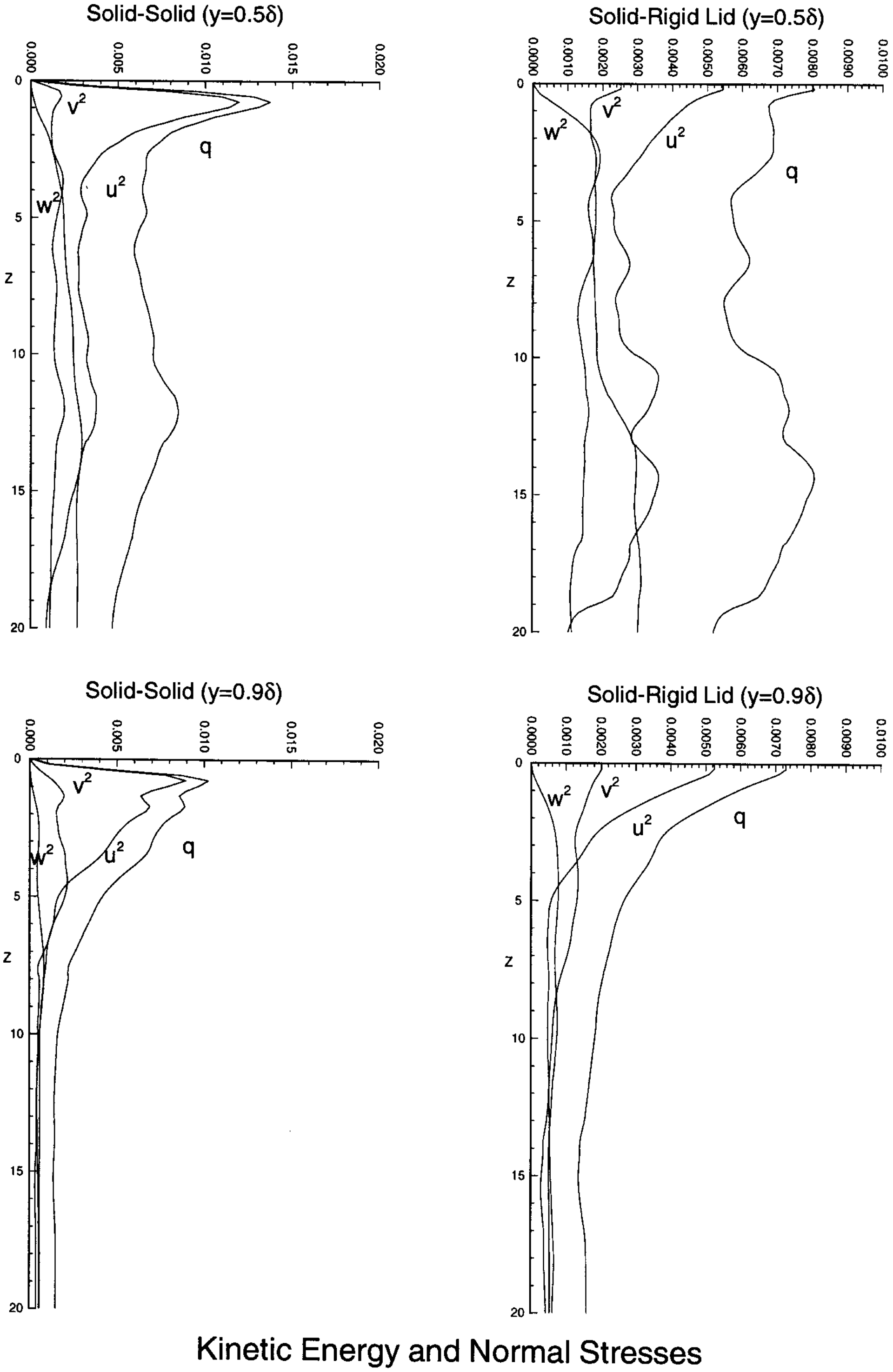

Figure 10. Variation of the turbulent kinetic energy for the solid–rigid-lid and the solid–solid juncture along the Z-axis at different Y locations.

4.3.5. Dynamic model. Recall that for computing the dynamic model coefficients, a box filter in physical space was used. For the initial part of the simulation, when periodic boundaries were applied in the spanwise as well as the streamwise directions, the model constants were averaged and held constant in the streamwise-spanwise plane. Thus the model coefficient was obtained as a function of time and the transverse direction. For the later part of the simulation, when the spanwise periodicity was relaxed, the model coefficient was averaged only in the streamwise direction, thus allowing it to vary in the spanwise direction in addition to the transverse direction and time. Figure 11 shows a representative distribution of the product of the model coefficient and the filter towards the end of the simulation. For the PBL, low values can be seen near the $Y=0$ wall boundary and also away in the far-field. In the case of SSC, the coefficient attains low values near the $Y=0$ and $Z=0$ boundaries which are both solid-walls. The distributions for the SRL and the SSC differ near the $Z=0$ boundary. The high values of model coefficient near the $Z=0$ boundary for SRL is due to the increase in the turbulent kinetic energy near the rigid-lid boundary.

It may be noted that in the present investigation, the mechanism for backscatter was not included and that is an area that needs attention, especially for solid–rigid-lid juncture flows. The reverse cascade of energy from small scales to large scales is important near the free-surface. Recently, Salvetti *et al.* [42] investigated this issue and developed a two parameter dynamic SGS model that combines the features of energy dissipation and backscatter to study decaying free-surface turbulence in open channel flows and obtained excellent comparisons with DNS.

5. CONCLUDING REMARKS

Results are reported of a LES performed to obtain a transitional-turbulent flow-field on a flat-plate boundary layer, and to study the turbulent flow in solid–solid and solid–rigid-lid junctures. Notwithstanding the approximations made, results indicate that temporal LES is capable of reproducing many of the experimentally observed features of the flow-fields studied. The results of the flat-plate simulation showed satisfactory agreement with the experimental measurements for the mean as well as for the turbulent quantities.

The turbulent flow-field generated on the flat-plate was then used to study turbulence in SSCs and SRLs by modifying the spanwise boundaries. The presence of the adjacent solid-wall/rigid-lid boundary significantly altered the mean and turbulent quantities, which in turn led to the formation of corner vortices driven by the gradients in Reynolds stresses. The relative sizes of the vortices and the general distribution of the anisotropy stress terms are in qualitative agreement with the available experimental data for the solid–solid juncture flow. The distribution of the mean quantities and the anisotropy terms showed remarkable similarity between the two juncture flow-fields. The main difference, however, was the absence of a second region of high vortical motion in the solid–rigid-lid corner. The significance of the asymmetry parameter in the formation of secondary vortices in juncture flows are discussed. Consistent with the experimental findings, the normalized anisotropy term exhibited similarity when plotted against the distance from the boundary, regardless of the type of boundary: solid-wall or rigid-lid. Moreover, the kinetic energy showed an increase as the rigid-lid boundary is approached, along with a redistribution of energy from the surface normal components to the other two components which is in agreement with the experimental observations of free-surface flows.

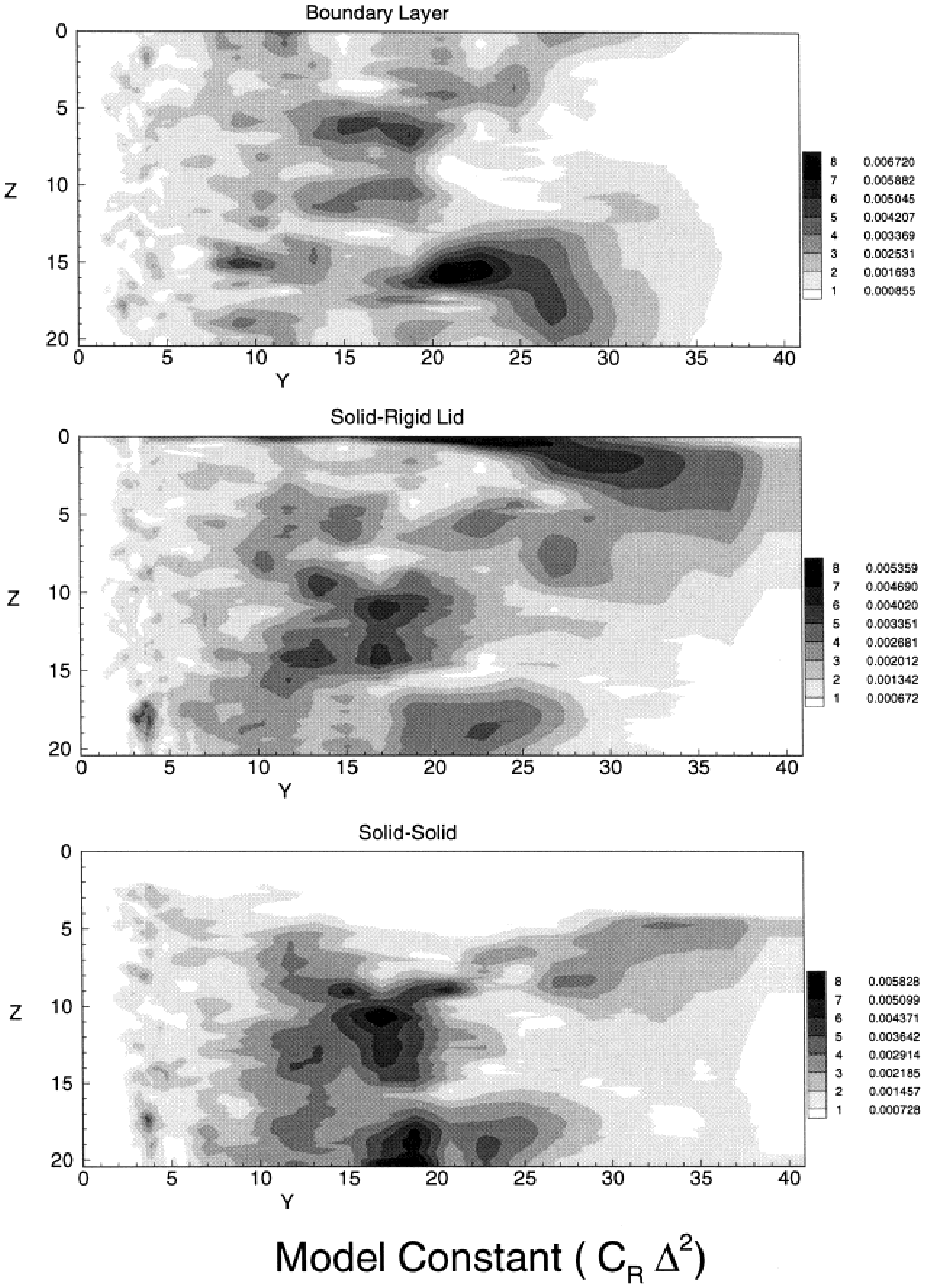

Figure 11. Contours of dynamic model constant in the YZ-plane, $C_R\Delta^2$.

The main limitations of the present work are the assumptions of temporal evolution of the flow-field, rigid-lid approximation for free-surface and the possible presence of compressibility effects. Temporal simulation of developing flows precluded sampling in time which severely limited the sample size. The presence of compressibility poses difficulties, especially when trying to approximate the free-surface with a rigid-lid boundary. The discrepancy with the data, such as the absence of a second vortical region and the differences in area of the vortical regions, could be due to these factors. Obviously further investigation is required to resolve these issues. For the solid–solid juncture there is no such ambiguity with the boundary conditions. However, even for the rigid-lid boundary, the behavior of kinetic energy and other quantities was very similar to those reported with fully incompressible simulations

Considering the complexity of the problem and the assumptions made, the overall results are significant and useful. For progress in this area, future work should involve the simulation of spatially developing flow with incompressible codes and more exact free-surface boundary conditions. Spatially developing flows allows sampling in time and hence a larger sample size is available for computing statistical correlations. While a fully deforming free-surface capability may not be feasible for LES/DNS studies in the near future, linearized free-surface boundary conditions can be easily implemented. There is also a need to adapt the two parameter dynamic subgrid-scale modeling procedure to account for the free-surface turbulence. Such simulations along with detailed experimental data are required to fully understand the physics of juncture flows, and are essential in the development of RANS turbulence models.

ACKNOWLEDGMENTS

This work is supported by the Office of Naval Research under Grant No. N00014-92-K-1092 under the administration of Dr. E.P. Rood. We acknowledge the support of the supercomputers at the Naval Oceanographic Office and the NASA Numerical Aerodynamic Simulation Program.

REFERENCES

1. M. Germano, U. Piomelli, P. Moin and W. Cabot, ‘A dynamic subgrid-scale eddy-viscosity model’, *Phys. Fluids A*, **3**, 1760–1765 (1991).
2. P. Bradshaw, ‘Compressible turbulent shear layers’, *Annu. Rev. Fluid Mech.*, **9**, 33–54 (1977).
3. J. Longo, H.P. Huang and F. Stern, ‘Solid/free-surface juncture boundary layer and wake, piercing flat plate’, *Exp. Fluids*, in press.
4. M.M. Rai and P. Moin, ‘Direct numerical simulation of transition and turbulence in a spatially evolving boundary layer’, *J. Comp. Phys.*, **109**, 169–192 (1993).
5. V.I. Kornilov and A.M. Kharitonov, ‘Investigation of the structure of turbulent flows in streamwise asymmetric corner configurations’, *Exp. Fluids*, **2**, 205–212 (1984).
6. M.M. Rai, T.B. Gatski and G. Erlebacher, ‘Direct numerical simulation of spatially evolving compressible turbulent boundary layers’, *AIAA*, **95-0583**, (1995).
7. P.R. Spalart, ‘Direct numerical simulation of a turbulent boundary layer up to $R_\theta = 1410$’, *J. Fluid Mech.*, **187**, 61–98 (1988).
8. P.R. Spalart and J.H. Watmuff, ‘Experimental and numerical study of a turbulent boundary layer with pressure gradients’, *J. Fluid Mech.*, **249**, 337–371 (1993).
9. P. Flohr and E. Balaras, ‘Large eddy simulation of a turbulent boundary layer’, Von Karman Institute Technical Note 187, (1995).
10. X. Wu, K. Squires and T. Lund, ‘Large eddy simulation of a spatially-developing boundary layer’, (personal communication), Proc. Supercomputing 1995, San Diego, December 1995.
11. U. Piomelli, T.A. Zang, C.G. Speziale and T.S. Lund, ‘Application of renormalization group theory to the large eddy simulation of transitional boundary layers’, in M.Y. Hussaini and R.G. Voigt (eds), *Instability and Transition*, Springer, Berlin, 1990, pp. 480–496.

12. F.F. Hatay and S. Biringen, 'Direct numerical simulation of low-Reynolds number supersonic turbulent boundary layer', *AIAA*, **95-0581**, (1995).
13. X. Normand and M. Lesieur, 'Numerical experiments on transition in the compressible boundary layer over an insulated flat plate', *Theor. Comput. Fluid Mech.*, **3**, 231–252 (1992).
14. C.G. Speziale, 'On turbulent secondary flows in pipes of non-circular cross-section', *Int. J. Eng. Sci.*, **20**, 863–872 (1982).
15. P. Bradshaw, 'Turbulent secondary flows', *Annu. Rev. Fluid Mech.*, **19**, 53–74 (1987).
16. Y. Miyake and T. Kajishima, 'Explanation of the origin of the secondary flow in a straight square duct on the basis of LES', in V.V. Kozlov and A.V. Dovgal (eds), *Separated Flows and* Jets, Springer, Heidelberg, 1991, pp. 149–152.
17. R.K. Madabhushi and S.P. Vanka, 'Large eddy simulation on turbulence driven secondary flow in a square duct', *Phys. Fluids A*, **3**, 2734–2745 (1991).
18. M.D. Su and R. Friedrich, 'Investigation of fully developed turbulent flow in a straight duct with large eddy simulation', *J. Fluids Eng.*, **116**, 677–684 (1995).
19. U. Schumann, 'Subgrid scale models for finite difference simulations of turbulent flows in plane channels and annuli', *J. Comput. Phys.*, **18**, 376–404 (1975).
20. K. Lam and S. Banerjee, 'Investigation of turbulent flow bounded by a wall and a free surface', *Proc. Annu. ASME Meeting*, Chicago, vol. 72, ASME, New York, 1988, p. 29.
21. R. Handler, J. Swearingen, T. Swean and R. Leighton, 'Length scales of turbulence near a free surface', *AIAA*, **91–01775** (1991).
22. T.F. Swean, R.I. Leighton, R.A. Handler and J. Swearingen, 'Turbulence modeling near the free surface in an open channel flow', *AIAA*, **91-0613** (1991).
23. N. Mangiavacchi, R. Gundlapalli and R. Akhavan, 'Dynamics of a turbulent jet interacting with a free surface', *Free-Surface Turbulence*, FED-vol 181, ASME Fluid Dynamics Conference, 1994, pp. 69–82.
24. S. Komori, R. Nagaosa and Y. Murakami, 'Direct numerical simulation of three-dimensional open-channel flow with zero-shear gas–liquid interface', *Phys. Fluids A*, **5**, 115–125 (1993).
25. D. Naot and W. Rodi, 'Numerical calculation of secondary motions in channel flow', *ASCE J. Hyd. Div.* **108**, 948–968 (1982).
26. R. Leighton, T. Wei and J.C. Neves, 'The secondary flow of the mixed boundary corner flow', *Free-Surface Turbulence*, FED-vol 181, ASME Fluid Dynamics Conference, 1994, pp. 15–24.
27. L.M. Grega, T. Wei, R.I. Leighton and J.C. Neeves, 'Turbulent mixed-boundary flow in a corner formed by a solid wall and a free surface', *J. Fluid. Mech.*, **294**, 17–46 (1995).
28. L.M. Logory, A. Hirsa and D.G. Anthony, 'Interaction of wake turbulence with a free surface', *Phys. Fluids*, **8**, 805–815 (1996).
29. T. Sarpkaya, M. Magee, M. Merrill and C. Merrill, 'Vortices, free-surface and turbulence', *Free-Surface Turbulence*, FED-vol 181, ASME Fluid Dynamics Conference, 1994.
30. M. Gharib, D. Dabiri and X. Zhang, 'Interaction of small scale turbulence with a free surface', *Free-Surface Turbulence*, FED-vol 181, ASME Fluid Dynamics Conference, 1994.
31. D.T. Walker, R.I. Leighton and L.O. Garza-Rios, 'Shear-free turbulence near a flat free surface', *J. Fluid. Mech.*, **320**, 19–51 (1996).
32. J. Smagorinsky, 'General circulation experiments with the primitive equations. I. The basic experiment', *Mon. Weather Rev.*, **91**, 99–164 (1963).
33. G. Erlebacher, M.Y. Hussaini, C.G. Speziale and T.A. Zang, 'Toward the large eddy simulation of compressible turbulent flows', *J. Fluid. Mech.*, **238**, 155–185 (1992).
34. M.K. Sreedhar, 'Large eddy simulation of turbulent vortices and mixing layers', *Doctoral Diss.*, Virginia Polytechnic Institute and State University, Blacksburg, VA, 1994.
35. M.K. Sreedhar and S.A. Ragab, 'Large eddy simulation of longitudinal stationary vortices', *Phys. Fluids*, **6**, 7 (1994).
36. K. Akselvoll and P. Moin, 'Application of the dynamic localization model to LES of turbulent flow over a backward facing step', *Eng. Appl. LES FED*, vol 162, ASME Fluid Dynamics Conference, 1993, pp. 1–6.
37. S. Ghosal, T. Lund, P. Moin and K. Akselvoll, 'A dynamic localization model for large eddy simulation of turbulent flows', *J. Fluid. Mech.*, **286**, 229–255 (1995).
38. D. Gottlieb and E. Turkel, 'Dissipative two-four methods for time-dependent problems', *Math. Comput.*, **30**, 703–723 (1976).
39. S.A. Ragab, S. Sheen, M.K. Sreedhar, 'An investigation of finite-difference methods for large eddy simulation of a mixing layer', *AIAA*, **92-0554**, (1992).
40. S. Biringen and W.C. Reynolds, 'Large eddy simulation of the shear free turbulent boundary layer', *J. Fluid. Mech.*, **103**, 53–63 (1981).
41. I. Nezu and H. Nakagawa, 'Turbulence in open-channel flows', *IAHR monogr.*, A. A. Balkema, Rotterdam, 1993.
42. M. Salvetti, Y. Zang, R.L. Street and S. Banerjee, 'Large eddy simulation of decaying free-surface turbulence with dynamic mixed subgrid-scale models', (personal communications), *Proc. 21st Symp. Naval Hydrodynamics*, *Trondheim*, *Norway*, *1996*, pp. 118–131.